

This is a copy of the published version, or version of record, available on the publisher's website. This version does not track changes, errata, or withdrawals on the publisher's site.

Enhanced electron acceleration by high-intensity lasers in extended (confined) preplasma in cone targets

D. R. Rusby, G. E. Cochran, A. Aghedo, et al.

Published version information

Citation: DR Rusby et al. Enhanced electron acceleration by high-intensity lasers in extended (confined) preplasma in cone targets. Phys Plasmas 30, no. 2 (2023): 023103

DOI: [10.1063/5.0127580](https://doi.org/10.1063/5.0127580)

This article may be downloaded for personal use only. Any other use requires prior permission of the author and AIP Publishing. This article appeared as cited above.

This version is made available in accordance with publisher policies. Please cite only the published version using the reference above. This is the citation assigned by the publisher at the time of issuing the APV. Please check the publisher's website for any updates.

This item was retrieved from **ePubs**, the Open Access archive of the Science and Technology Facilities Council, UK. Please contact epublications@stfc.ac.uk or go to <http://epubs.stfc.ac.uk/> for further information and policies.

Enhanced electron acceleration by high-intensity lasers in extended (confined) preplasma in cone targets

Cite as: Phys. Plasmas **30**, 023103 (2023); <https://doi.org/10.1063/5.0127580>

Submitted: 22 September 2022 • Accepted: 14 December 2022 • Published Online: 08 February 2023

 D. R. Rusby,  G. E. Cochran,  A. Aghedo, et al.



View Online



Export Citation



CrossMark

ARTICLES YOU MAY BE INTERESTED IN

[Gamma-ray imaging of inertial confinement fusion implosions reveals remaining ablator carbon distribution](#)

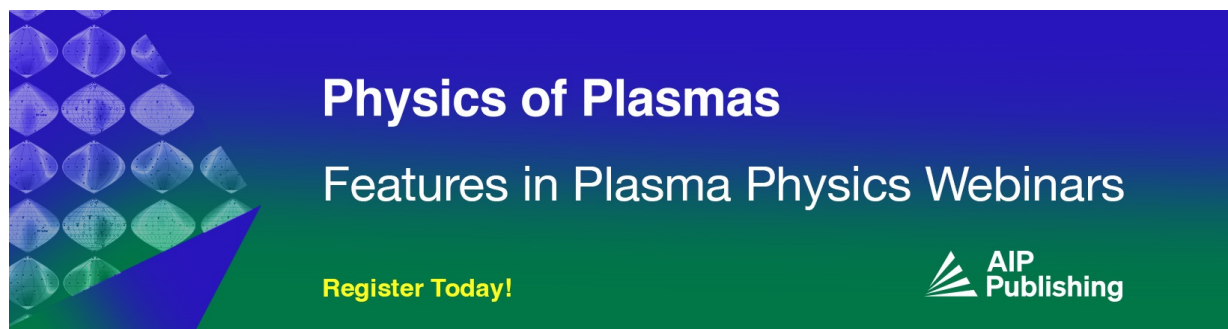
Phys. Plasmas **30**, 022703 (2023); <https://doi.org/10.1063/5.0122938>

[Perspectives on relativistic electron-positron pair plasma experiments of astrophysical relevance using high-power lasers](#)

Phys. Plasmas **30**, 020601 (2023); <https://doi.org/10.1063/5.0134819>


[Development of a bright MeV photon source with compound parabolic concentrator targets on the National Ignition Facility Advanced Radiographic Capability \(NIF-ARC\) laser](#)

Phys. Plasmas **30**, 013101 (2023); <https://doi.org/10.1063/5.0124539>



Physics of Plasmas
Features in Plasma Physics Webinars

Register Today!



Enhanced electron acceleration by high-intensity lasers in extended (confined) preplasma in cone targets

Cite as: Phys. Plasmas **30**, 023103 (2023); doi: 10.1063/5.0127580

Submitted: 22 September 2022 · Accepted: 14 December 2022 ·

Published Online: 8 February 2023



View Online



Export Citation



CrossMark

D. R. Rusby,^{1,a)} G. E. Cochran,¹ A. Aghedo,² F. Albert,¹ C. D. Armstrong,³ A. Haid,⁴ A. J. Kemp,¹ S. M. Kerr,¹ P. M. King,^{1,5} N. Lemos,¹ M. J.-E. Manuel,⁴ T. Ma,¹ A. G. MacPhee,¹ I. Pagano,⁵ A. Pak,¹ G. C. Scott,¹ C. W. Siders,¹ R. A. Simpson,^{1,6} M. Sinclair,⁷ S. C. Wilks,¹ G. J. Williams,¹ and A. J. Mackinnon¹

AFFILIATIONS

¹Lawrence Livermore National Laboratory, Livermore, California 94550, USA

²Department of Physics, Florida A & M University, Tallahassee, Florida 32307, USA

³Central Laser Facility, Rutherford Appleton Laboratory, Didcot OX11 0QX, United Kingdom

⁴General Atomics, La Jolla, California 92093, USA

⁵Department of Physics, University of Texas at Austin, Austin, Texas 78712, USA

⁶Department of Nuclear Science and Engineering, Massachusetts Institute of Technology, Cambridge, Massachusetts 02139, USA

⁷Department of Physics, University of California at Los Angeles, Los Angeles, California 90095, USA

^{a)} Author to whom correspondence should be addressed: rusby1@llnl.gov

ABSTRACT

We report on experimental results from a high-intensity laser interaction with cone targets that increase the number ($\times 3$) and temperature ($\times 3$) of the measured hot electrons over a traditional planar target. This increase is caused by a substantial increase in the plasma density within the cone target geometry, which was induced by 17 ± 9 mJ prepulse that arrived 1.5 ns prior to the main high intensity ($> 10^{19}$ W/cm²). Three-dimensional hydrodynamic simulations are conducted using HYDRA which show that the cone targets create substantially longer and denser plasma than planar targets due to the geometric confinement of the expanding plasma. The density within the cone is a several hundred-micron plasma “shelf” with a density of approximately 10^{20} n_e/cc. The HYDRA simulated plasma densities are used as the initial conditions for two-dimensional particle-in-cell simulations using EPOCH. These simulations show that the main acceleration mechanism is direct-laser-acceleration, with close agreement between experimentally measured and simulated electron temperatures. Further analysis is conducted to investigate the acceleration of the electrons within the long plasma generated within a compound parabolic concentrator by the prepulse.

Published under an exclusive license by AIP Publishing. <https://doi.org/10.1063/5.0127580>

I. INTRODUCTION

The interaction between a high-intensity laser ($> 10^{18}$ W/cm²) and a solid target and the subsequent acceleration of electrons to relativistic energies is a non-linear and complex process and depends on many laser and target parameters. One of the key parameters is the extent of the preplasma that forms on the front surface prior to the main pulse of the laser arrival.^{1–5} In a laser–solid interaction, the laser-pedestal courtesy of amplified spontaneous emission (ASE) or a prepulse of the main laser is often intense enough to ionize the front surface of the target, forming an expanding plasma. If the density gradient of the plasma is steep, then the electrons in the plasma are exposed briefly to the laser fields before the laser reaches the critical density,

$n_c = \epsilon_0 \gamma m_e \omega_L^2 / e^2$, at which point the laser cannot propagate further. The γ factor here is when the electron mass is increased due to its relativistic velocity within the laser field. The energy exchange between the electrons and laser in this regime is dominated by the ponderomotive force. This leads to an electron distribution whose temperature can be described by the ponderomotive scaling,⁶ $T_{pond} = m_e c^2 (\sqrt{1 + a_0^2/2} - 1)$, where a_0 is the normalized vector potential given as $a_0 \approx 0.85 \sqrt{I_{18} \lambda_\mu^2}$, I_{18} is the intensity in units of 10^{18} W/cm², and λ_μ is the wavelength of the laser in micrometers; for reference, an electron temperature of ~ 1 MeV would require a laser intensity of just over 10^{19} W/cm² for a laser wavelength of 1 μ m. Numerous empirical and

analytical electron temperature “scaling laws” exist in the literature,^{7,8} which all share similar relationship to $I_{18}\lambda^2$. Intensity scaling studies have been conducted and broadly agree with these scaling laws.^{9–12} Constrained by these scaling laws, achieving electron temperature greater than a few MeV requires intensities above 10^{20} W/cm² for a laser wavelength of 1 μ m.

However, while some experimental observations followed the ponderomotive or similar scalings very closely, some did not. Experimental campaigns where the pulse duration is long^{13,14} and/or where there is an induced scale length^{1–3,15} measured electron (and/or protons) energies that far exceed the limits set by the ponderomotive scaling.

If the extent of the plasma is much longer than tens of micrometers, the electrons can be directly exposed to the laser field over multiple laser cycles. An electron that is injected into the propagating laser field can accelerate to much higher energies than described by the free electron ponderomotive limit and yield much higher temperatures for modest laser intensities. This is often referred to as Direct Laser Acceleration (DLA).^{4,16–19} As well as the plasma playing a significant role in the generation of these electrons, the duration of the laser pulse is also important. In the multi-picosecond regime, the front surface plasma can evolve during the duration of the pulse leading to the expansion²⁰ and/or modifications to the plasma.⁴ Furthermore, longer laser pulse can give rise magnetic fields that aid in the injection of electrons into the laser field^{20,21} to undergo DLA.

Although the electron temperature from DLA can vary for a given laser intensity, the scaling generated via simulations by Pukhov *et al.*¹⁹ can be used to demonstrate the increase in electron temperature compared to the ponderomotive scaling. For example, the electron temperature from the ponderomotive scaling for an intensity of 10^{19} W/cm² and a laser wavelength of 1 μ m is ~ 0.95 MeV, whereas the Pukhov scaling yields an electron temperature of ~ 4.7 MeV: approximately five times the ponderomotive scaling.

The capability of generating multi-MeV electron temperatures that far exceed the scaling laws for $10^{18–19}$ W/cm² intensities is of particular interest for fixed geometry/intensity limited systems, such as NIF-ARC, or secondary source generation. For example, the generation of MeV x rays for nondestructive imaging of high areal density objects is both dependent on the electron temperature and the laser energy coupled to the electrons.^{22–26} Furthermore, the maximum achievable proton energy from Target Normal Sheath Acceleration (TNSA) is proportional to the electron temperature^{27–29} and DLA electrons can sustain the maximum proton energy at modest laser intensities.¹⁵ The experimental study and optimization of DLA are, therefore, of much interest.³⁰

Target geometry can be used as an effective method to increase the plasma scale length. Cone targets have been investigated under many different laser conditions and are a promising method of enhancing the electron production through a variety of methods,^{10,31} and as such were of great interest for electron fast ignition research.^{32,33} However, cone or conical targets can be highly effective at creating longer scale lengths due to a confinement up of the plasma by restricting the plasma expansion laterally. The plasma growth and subsequent acceleration of high energy electrons were seen as a problem as it led to energy being deposited far from the targeted region. Nevertheless, the plasma growth within the cone targets can lead to much longer plasma scale lengths which can be used to optimize the DLA process.

We have chosen to use a Compound Parabolic Concentrator (CPC) as the target for this experiment.^{34,35} The CPC is designed to reflect laser energy that enters the opening aperture toward the tip via a single bounce. As the tip of the CPC is much smaller than the opening aperture, this leads to a higher laser intensity at the tip. In a low prepulse scenario, the CPCs have been shown empirically to yield hotter electron temperature that is proportional to the increase in the intensity at the tip.¹² In the situation where prepulse/ASE is such that a preplasma can be generated, a CPC target can increase that preplasma in two ways. In a similar manner to which the main pulse of the laser will be intensified by the geometry of the CPC, as will any laser energy that arrives prior to the main pulse, potentially leading to a hotter sub-critical plasma to form and grow at the tip.³⁶ As the plasma expands, the lateral expansion will be hindered by the geometry of the CPC, causing the plasma to expand further away from the target. While a similar effect would occur within straight narrow capillaries, it is much more difficult to direct all of the laser energy in a narrow tube compared to a CPC which has a large opening aperture. The intensity enhancement combined with the lateral confinement of the plasma will lead to a much longer scale length than when using a planar/flat target. Previous results presented by Williams *et al.*¹³ using CPCs at NIF-ARC show an increase in emitted electrons and positrons over the planar target case. Numerical, hydrodynamic simulations show that the CPCs generate a moderate scale length which is longer than the planar target.

Here, we present experimental results from the Titan Laser at the Jupiter Laser Facility (JLF), where we induce a long scale length using a prepulse approximately 1.5 ns prior to the main pulse. We compare the electron production from three targets: two CPCs with different tip diameters (25 and 50 μ m) and a planar target. The two CPC targets show a substantial increase in the number of electrons above 5 MeV ($\sim \times 20$) and an overall increase in the electron temperature ($\sim \times 2$), with the highest electron temperature recorded from the smaller CPC tip size, yielding a temperature of ~ 21 MeV. The measured temperatures are much higher than the ponderomotive temperature for the intensity of laser used, suggesting that these electrons are likely the result of DLA within a long plasma. The expansion of plasma induced by the prepulse is modeled numerically using the hydrodynamic code HYDRA, which demonstrates that the CPCs help create a much longer scale length. In particular, there is a formation of a plasma sheath that extends for hundreds of micrometers at electron densities of approximation $n_e \sim 4 \times 10^{19}$ /cc ($\sim 0.04n_c$). Two-dimensional Particle-in-Cell (2D PIC) simulations between the main-pulse and the modeled plasma for each of the targets are conducted. The additional plasma within the CPCs is beneficial to the generation of high energy electrons which leads to an increase in total electron energy and temperature. Further particle tracking analysis shows that the self-focusing and filamentation within the plasma aids in the generation of the highest energy electrons.

II. EXPERIMENTAL PROCEDURE

The experimental campaign was conducted at the Titan laser at the Jupiter Laser Facility at the Lawrence Livermore National Laboratory. The Titan laser delivered 129 ± 21 J on a target during the campaign. A measurement of the pulse duration was made using autocorrelation yielding 0.8 ± 0.2 ps. The beam was focused using a F/10 off-axis parabolic to create a large focal spot and narrower angle of

incoming beam such that a long CPC would be suitable. The measured vacuum focal spot had a 50% energy enclosed radius of $19 \pm 2 \mu\text{m}$. The average peak intensity during the campaign was $\sim 1.4 \times 10^{19} \text{ W/cm}^2$.

The aforementioned prepulse was characterized using a pickoff of the main beam from the laser-compressor and measured using a water-cell and photodiode.³⁷ The average measured prepulse is shown in Fig. 1 with the shaded region representing two times the standard deviation. Integrating under the prepulses only, the average total energy contained within the recorded prepulses was $17 \pm 9 \text{ mJ}$ and arrived approximately 1.5 ns before the diode saturates due to the main pulse. This equates to an intensity of $5.2 \pm 2.5 \times 10^{19} \text{ W/cm}^2$.

The CPC geometry was initially described by Hinterberger and Winston in 1966.³⁴ The application of CPC being utilized for high-intensity lasers was first described by Macphee *et al.* where they were used on NIF-ARC.³⁵ Figure 2 has a schematic of the CPC geometries used here.

The experimental setup of the Titan chamber is shown in Fig. 3. The primary diagnostics during this campaign are the three electron-positron proton spectrometers (EPPSs) located at 12° , 48° , and 56° from the laser axis. The EPPS is sensitive to electrons greater than 2 MeV and up to 150 MeV. The combination of three EPPSs enables a better diagnosis of the accelerated electrons, providing angular information about electron temperature and number. The EPPS utilizes an image plate that has a well understood sensitivity to electrons.³⁸

Finally, to measure the production of high energy x rays ($>10 \text{ MeV}$), an angular nuclear activation measurement was performed using nickel which was only performed on two shots. Further details on this measurement are provided in Sec. III.

III. EXPERIMENTAL RESULTS

The electron spectra captured on the EPPS positioned at 12° from the laser axis are shown in Figs. 4(a)–(c) for the planar, $25 \mu\text{m}$ CPC, and $50 \mu\text{m}$ CPC, respectively. The electron temperature, T_e , of each spectrum is fitted using a single Boltzmann distribution (Ae^{-E/T_e}) at energies above 15 MeV. This value is chosen to start above the initial bump in the spectra, which is likely caused by the

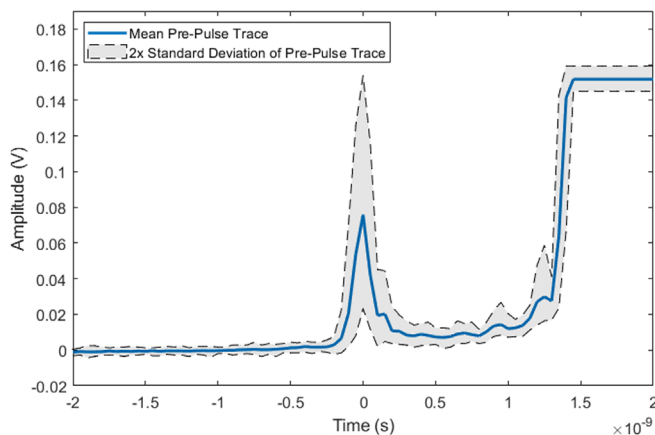


FIG. 1. The dashed shaded region represents two times the standard deviation, which encompasses all of the prepulses measured. The right of the trace, at approximately 1.5 ns, the trace saturates. This represents the main pulse of the laser. The mean prepulse (blue) of the prepulses recorded during this experiment was $17 \pm 9 \text{ mJ}$.

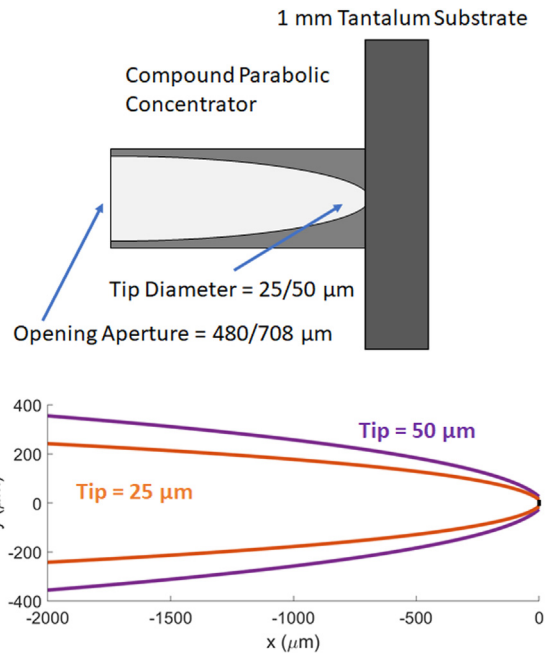


FIG. 2. Illustration of the Compound Parabolic Cones (CPCs) attached to the tantalum substrate. An accurate geometry of the CPC internal walls is plotted with a 1:1 aspect ratio for the two CPC geometries used in this study.

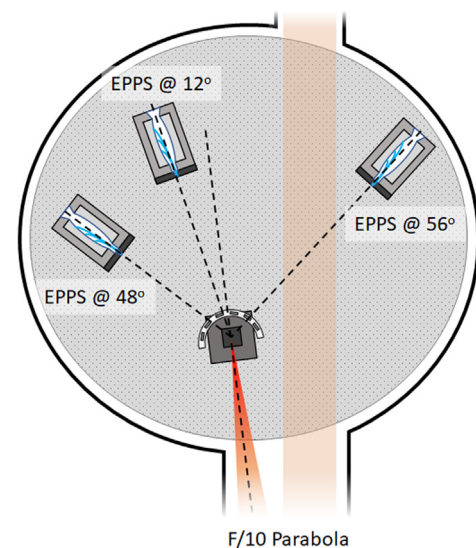


FIG. 3. Schematic of the experimental campaign. The parabolic focusing optic is positioned external to the main chamber to incorporate the long focal length. Three electron spectrometers (EPPSs) diagnostics are positioned around the interaction.

electrostatic fields that form on the target creating a potential that restricts the escaping electron population.^{39,40} The average temperature recorded on the EPPS 12° from laser axis for the planar, $25 \mu\text{m}$ CPC, and $50 \mu\text{m}$ CPC is 5.7 ± 2.8 , 14.1 ± 7.1 , and $13.3 \pm 4.5 \text{ MeV}$, respectively. The uncertainty in the electron temperature is taken from

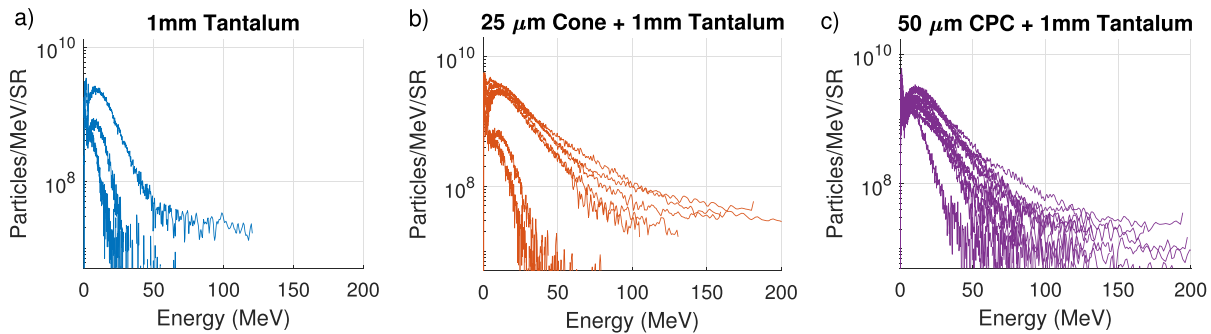


FIG. 4. Electron spectra obtained at 12° from laser axis on the EPPS. (a)–(c) show the spectra taken on 1 mm tantalum, 25 μm CPC with 1 mm tantalum, and 50 μm CPC with 1 mm tantalum.

the standard deviation of all the recorded spectra. We observe a large uncertainty for the 25 μm CPC target; from Fig. 4(b), it is clear that for some shots the electron spectra are similar to the spectra measured from the planar target. It is likely that for these shots, at least part of the laser beam did not enter the CPC, possibly hitting the entrance of the CPC. Unfortunately, no diagnostics were implemented to diagnose the on-shot pointing of the laser into the CPC opening aperture; therefore, we cannot definitely conclude that these spectra are caused by mispointing. We include these shots in our results as such.

Angular plots of the average temperature and number of electrons per steradian are created using the three EPPSs shown in Fig. 5. The error bars on each plot represent the standard deviation of the data. While it may not be true that there is no electron emission at −90° and 90°, we observe that the data electron yielded measured at the larger angles is typically lower than the data recorded at 12°. Therefore, to anchor the Gaussian fit (dashed lines), the electron temperature and number are set to 0 at −90° and 90°. The electron temperature appears much broader/more uniform as a function of angle than the number of electrons, whose distribution is narrower. The Full-Width-Half-Maximum (FWHM) of the average fits for the integrated number of electron for the planar, 25 μm CPC, and 50 μm CPC are 70.6°, 72.4°, and 88.4°, respectively. Previous experimental data using diagnostics with far more angular sensitivity have shown similar measurements for the angular distribution of the high energy electron beam.^{41,42}

While the average data suggest that the electron beam points along the laser axis, some individual shots demonstrate this not to be the case always. Pointing variations in the electron beam within the CPCs can be caused by the pointing fluctuations of the laser relative to the CPC. This has been shown previously using PIC simulations.¹² Additionally, long plasma (see Secs. V and VI) can cause hosing instabilities in the laser which can steer the electron distributions.⁴¹

Two shots were taken to diagnose the high energy x rays using ⁵⁸Ni(γ,n)⁵⁷Ni photo-nuclear reactions which has a threshold of >10 MeV. Six nickel samples are placed around the target separated by 15° to enable an angular measurement of the high energy x rays. ⁵⁷Ni emits several characteristic lines, primarily 161, 511 (via annihilation), and 1377 keV. The samples are counted at the Lawrence Livermore Nuclear Counting Facility, using calibrated Sodium Iodide (NaI) scintillators. This setup was deployed during a planar target and 50 μm CPC shot. The measured number of ⁵⁷Ni atoms at T₀ is plotted as a function of angle in Fig. 6. The error bars on the angular

distribution are from the size of the sample and the uncertainty of the counting. As these activation data are primarily sensitive to x rays with energies greater than 10 MeV, this shows that there are many more high energy x rays produced when using the CPC target which is

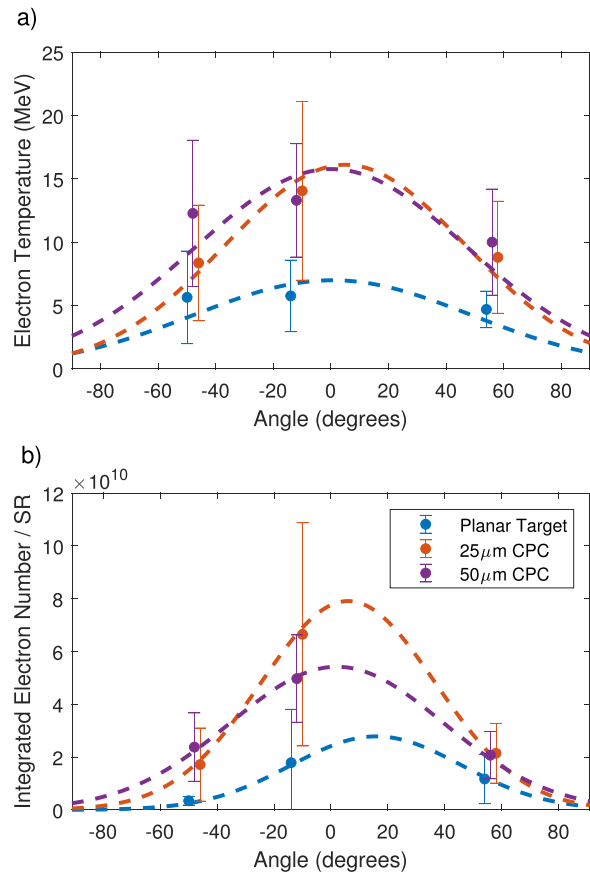


FIG. 5. Angular plots of the (a) mean electron temperature and (b) mean electron number for all data recorded on three EPPSs positioned at approximately 12°, 48°, and 56° from laser axis for the three different target types. The dotted lines represent a Gaussian fit of the mean data and the solid line represents the standard deviation of the data. The points are slightly offset from the measured locations in order to display the extents of the uncertainties.

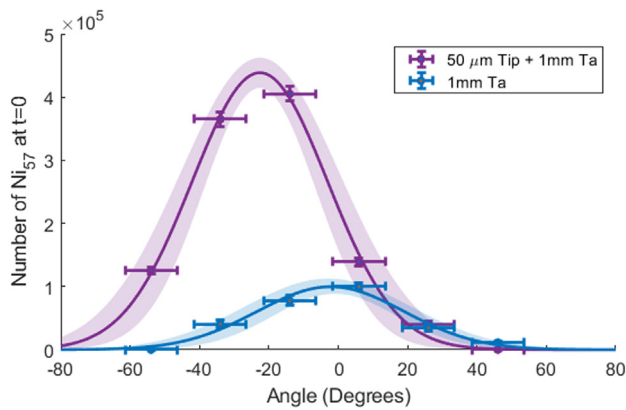


FIG. 6. Angular distribution of the nickel activation measured from two shots: a $50\text{ }\mu\text{m}$ CPC and a planar target. The activation is induced by greater than 10 MeV x rays from the interaction. A Gaussian fit is calculated for both sets of data. The Full Width Half Maxima (FWHM) is $55.3 \pm 9.2^\circ$ for the CPC and $60.0 \pm 8.8^\circ$ for the planar target, respectively. There is approximately four times more activation when using the CPC target. The angular uncertainty represents the angular size of the samples.

consistent with the electron spectral measurements. A Gaussian distribution is fit to the data and the Full Width Half Maxima (FWHM) is $55.3 \pm 9.2^\circ$ for the CPC and $60.0 \pm 8.8^\circ$ for the planar target, respectively. These angular measurements are similar to those measured from previous experiments that have performed x-ray measurements using nuclear activation.^{5,43,44}

IV. EXPERIMENTAL RESULTS DISCUSSION

The electron temperatures observed from the experiment are much higher than the ponderomotive scaling for the input laser intensity. For the planar target, our measured temperature $5.7 \pm 2.8\text{ MeV}$ is close to the predicted temperature for the Puhkov scaling, 6.7 MeV . Previously, for CPCs without a significant prepulse, the observed temperature enhancement could be calculated by using a simple geometric focusing equation, similar to that shown for focusing plasma mirrors.¹² This equation considers both the increase in intensity via the focusing and the utilization of the energy of the beam captured by CPC geometry and is expressed as $I_{\text{enhance}} = (R_{\text{FocalSpot}}^2/R_{\text{Tip}}^2) \times (E_{\text{CPC}}/E_{>118})$, where $R_{\text{FocalSpot}}$ is the size of the focal spot, R_{Tip} is the CPC tip size, E_{CPC} is the energy that enters the opening aperture of the CPC, and $E_{>118}$ is the original proportion of the energy above the approximate relativistic limit for electron oscillations. The electron temperature then follows: $T_e \propto I_L \times I_{\text{enhance}}$, where I_L is the estimate of the laser intensity. The intensity enhancement is expected to be approximately 8 for given the focal spot and the $25\text{ }\mu\text{m}$ tip CPC. Applying this enhancement to the intensity and using the Puhkov scaling yield a temperature in the region of 18 MeV , similar to the experimentally measured value for this CPC $14.1 \pm 7.1\text{ MeV}$. However, as Williams *et al.*¹³ showed using hydro and PIC simulation, the intensification of the CPCs can be almost completely nullified by the presence of a pre-formed plasma. We will, therefore, perform a similar investigation to determine the effect of focusing and plasma within the CPC.

Typically, a transverse optical probe is used to measure the plasma density. However, as the CPC wall material is opaque, an optical probe cannot diagnose the plasma at the CPC tip. An analytical

approximation, similar to that applied by Simpson *et al.*,¹⁵ can be applied here assuming that the CPC intensifies the prepulse via a similar methodology demonstrated previously for CPCs.¹² However, while this is applicable to planar targets, predicting a scale length of $146 \pm 12\text{ }\mu\text{m}$, it does not consider the geometric confinement from the walls of the CPC. Instead, we use the massively parallel, three-dimensional (3D) radiation-hydrodynamics code HYDRA to model both the increase in intensity due to geometric focusing in 3D and plasma growth due to the geometric confinement.

V. HYDRA SIMULATIONS

Our hydro simulations of the prepulse were chosen to closely mimic the experimental recorded prepulses (see Fig. 1). The prepulse had a 700 fs FWHM temporal profile with an integrated energy of 24 mJ . The plasma is allowed to expand for 1.5 ns as experimentally the prepulse was consistently measured to arrive 1.5 ns before the main pulse. Both CPCs and a planar were simulated and initialized as solid density plastic with a small hydrogen preplasma.

To reduce simulation time, radiation and electron conduction were not employed and a single temperature model was used for ions and electrons. There are 20 angular bins for an angular resolution of 18° per bin; the simulation extends approximately $1100\text{ }\mu\text{m}$ past the cone opening.

Electron density maps for the three simulations are shown in Fig. 7. The simulated density of the planar target appears relatively uniform over the laterally extent of the focal spot and can be fit using multiple scale lengths. The longest of the scale lengths can be fit using a scale length of approximately $125\text{ }\mu\text{m}$ which is similar to the predicted value from the analytical estimation used by Simpson *et al.*¹⁵ The densities within the two CPCs appears much denser. Lineouts of the density, averaged angularly within a $100\text{ }\mu\text{m}$ radius, are shown for all cases in Fig. 8. The results from the two CPC targets have vastly different density profiles to the flat target case. Rather than the typical decaying exponential often observed from planar targets from both experiments^{1,2,5} and hydrodynamic simulations,^{14,45,46} the density profiles appear to have plateau profile at a density of roughly $4 \times 10^{19}\text{ n}_e/\text{cc}$. After the density plateau, the density quickly drops to densities similar to that of the planar target.

There are differences between the two densities from the CPCs. The density plateau is approximately $100\text{ }\mu\text{m}$ longer for the $25\text{ }\mu\text{m}$ CPC. This is likely due to the additional geometric confinement of the plasma not only within the smaller CPC but also within the HYDRA there is a higher temperature observed within the $25\text{ }\mu\text{m}$ plasma. These two effects likely lead to a longer plasma.

VI. PARTICLE-IN-CELL SIMULATIONS

The plasma densities shown within the black dashed boxes in Fig. 7 are used as the initial density conditions for 2D Particle In Cell simulations. The PIC simulations are performed using code EPOCH, an explicit, relativistic PIC code. The simulation box for the flat target is smaller than the two CPC boxes. The flat simulation starts at $-300\text{ }\mu\text{m}$ and the CPC simulations start at $-550\text{ }\mu\text{m}$. The resolution of the simulation in the x-direction is $\sim \lambda/20$ and in the y-direction is $\sim \lambda/16$, where λ is the laser wavelength, $1.056\text{ }\mu\text{m}$. Due to the large size of the simulation box and number of cells ($\sim 2.9 \times 10^7$) and in order to make the simulations computationally viable, only ten particles per cell are used and the density is limited to $5 \times n_{\text{crit}}$. The laser

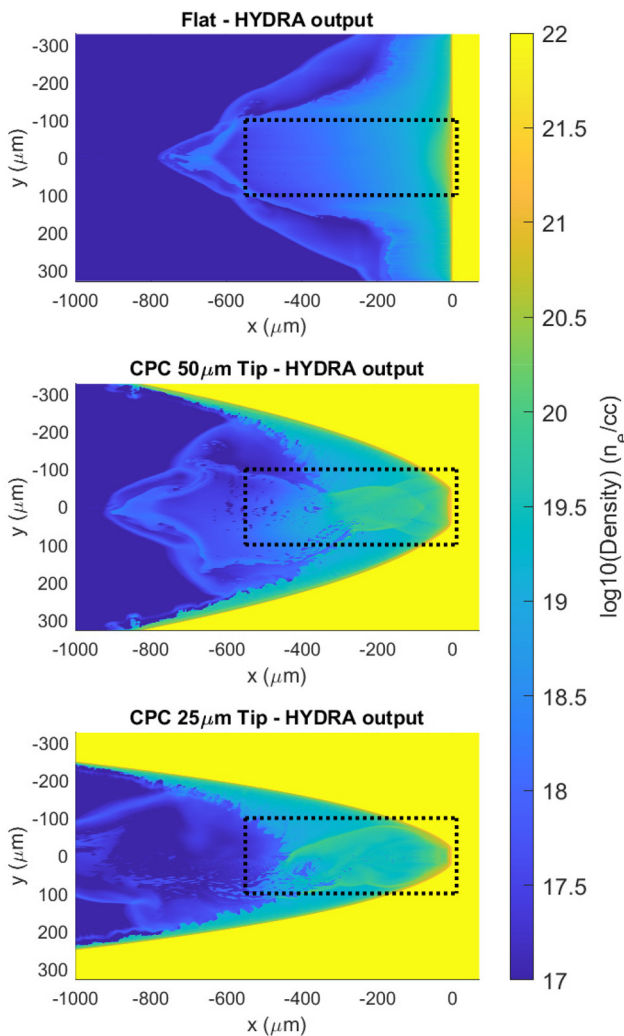


FIG. 7. Slices of HYDRA simulations showing the electron densities of the three different targets using a 24 mJ prepulse. The CPC confine the plasma, yielding to a high on-axis electron density leading to a higher density within the CPCs. The longest scale length on the planar target has an electron density similar to the analytical prediction from Simpson *et al.*¹⁵ The boxes represent the regions used to conduct 2D particle-in-cell simulations (see Sec. VI).

pulse has a peak intensity of 2×10^{19} W/cm² with a Gaussian temporal profile with a FWHM of 700 fs and a Gaussian spatial profile with a FWHM of 38 μm in the y-direction.

Snapshots of the intensity profiles for the three simulations are shown in Fig. 9 at the time the laser reaches the critical surface. We observe no intensification due to the geometry of the CPC in Figs. 9(b) and 9(c), but we do observe self-focusing and filamentation effects that yield higher intensities than the input intensity. We observe intensities up to 6×10^{19} W/cm². The filamentation growth within the CPC plasma is much greater than the planar target case. Observing the intensity maps through the simulation, these filaments form as the laser reaches plasma densities of roughly $n_e = 1 \times 10^{19}$ /cc. For the CPC simulations, this locates to where the plasma plateau begins.

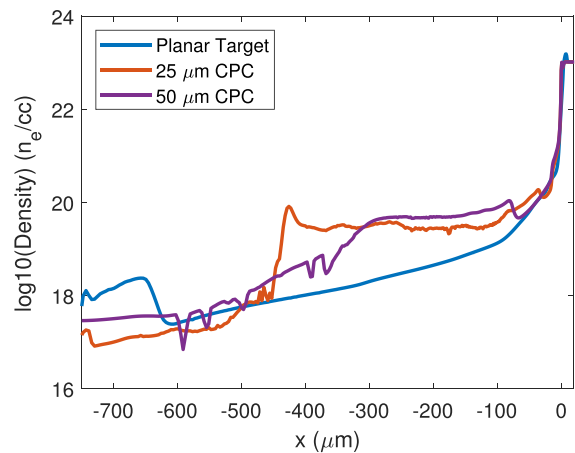


FIG. 8. Central lineouts of the HYDRA simulations in Fig. 7 showing the electron densities of the three different targets.

The electron spectra for all three simulations are plotted in Fig. 10 with the temperatures of the electron distributions listed in the legend. Also, for reference, the ponderomotive scaling predicted electron temperature for the input peak laser intensity of 2×10^{19} W/cm² is also

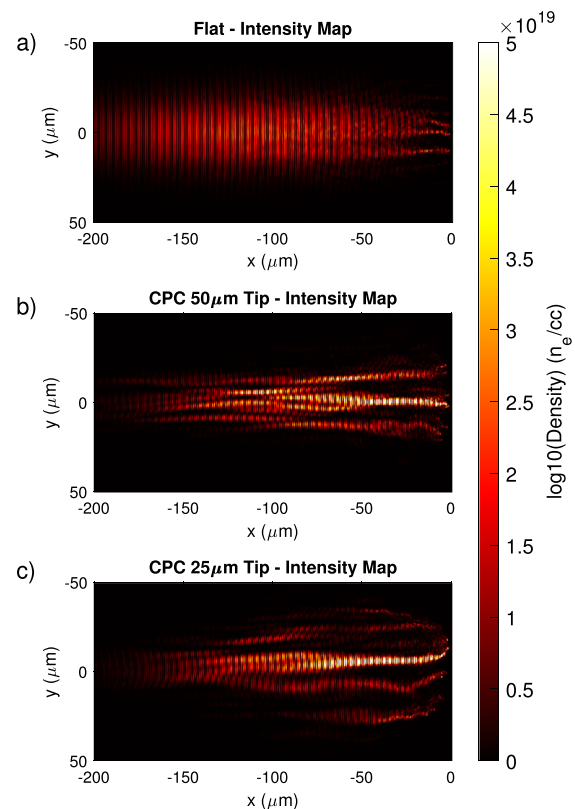


FIG. 9. Intensity maps of the three simulations: (a) flat, (b) 50 μm CPC, and (c) 25 μm. The laser within the plasmas of the two CPC targets filaments much more than the planar target. Within these filaments, the peak intensity is much higher than the input peak intensity.

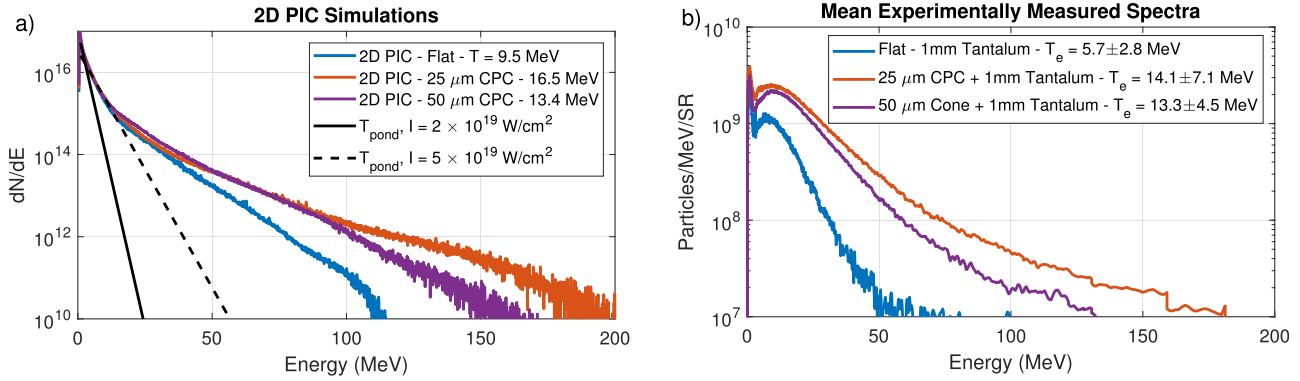


FIG. 10. Electron spectra from flat and cone targets. (a) Simulated spectra recorded at $x > 50 \mu\text{m}$. (b) Measured mean escaping electron spectra. Note that simulated spectra do not experience a self-consistent potential building up around the target, see the “bump” at 10 MeV.

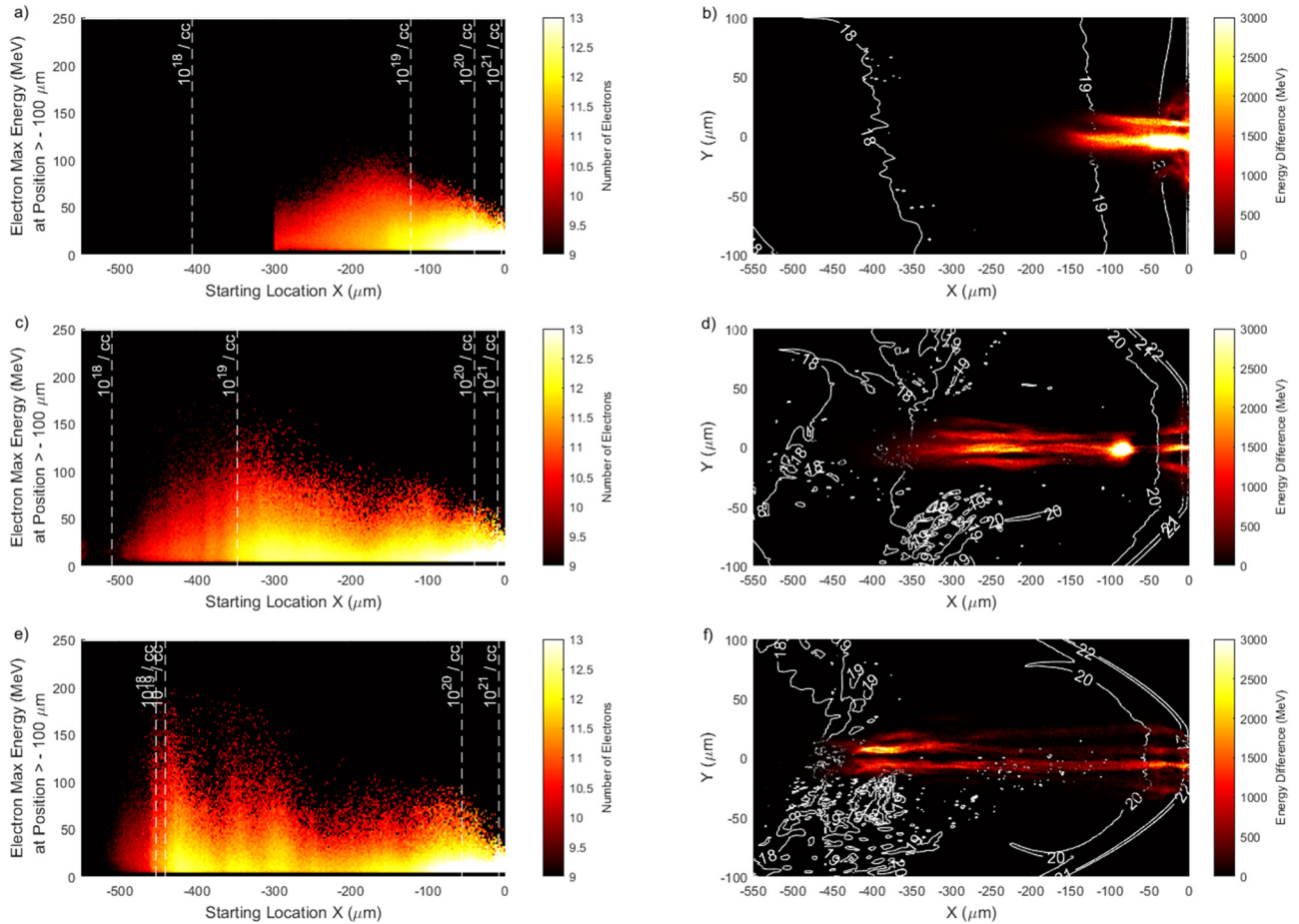


FIG. 11. The maximum energy that an electron obtains is plotted as a function of that electrons starting location for the flat target, $50 \mu\text{m}$ CPC, and $25 \mu\text{m}$ CPC simulations in (a), (c), and (e), respectively. Also, the plots are the initial locations of the densities $n_e = 10^{18,19,20,21}/\text{cc}$ taken from the horizontal lineouts in Fig. 8. The electrons that gain the highest energies are the electrons that start further away from the target and roughly after $n_e = 10^{19}/\text{cc}$. The locations where the electrons gain energy are plotted in (b), (d), and (f) for the flat, $50 \mu\text{m}$ CPC, and $25 \mu\text{m}$ CPC simulations, respectively. Labeled density contours are also plotted. The labels represent the orders of the initial electron density. Much of the energy gain by the electrons occurs within long narrow regions which represent the locations of the filaments within the simulation.

plotted and matched to the amplitudes of the spectra. Due to the filaments and the self-focusing within the plasma, where the local peak intensity can exceed $5 \times 10^{19} \text{ W/cm}^2$, an additional line is plotted that is two times the ponderomotive temperature that closely matches the spectra up to 25 MeV. At the highest energies, we observe that all three simulations yield electrons temperatures much higher than the ponderomotive temperature. The temperatures for the planar, 25 μm CPC, and 50 μm CPC are 9.5, 13.4, and 16.5 MeV, respectively.

The average experimentally measured electron spectra is plotted in Fig. 10(b). The trend in the temperature is similar between the experimental and simulated electron spectra. However, the vast increase in the experimentally measured electron yield between the planar and CPC targets, particularly between 10 and 50 MeV, is not well reproduced in the simulations.

To better understand the acceleration of electrons, further analysis using particle tracking is used. As the highest energy electrons are likely to be generated via the DLA mechanism, we expect that the highest energy electron is accelerated over multiple laser cycles and there should be a relationship between where an electron begins accelerating and the energy it can achieve before entering the target. 10^5 electrons that reach energies greater than 15 MeV are tracked back to their starting location (the location that they first appear in our outputs). The final energy each electron achieves is plotted as a function of its starting location for each simulation in Figs. 11(a), 11(c), and 11(e) for the planar, 25 μm CPC, and 50 μm CPC, respectively. Between the densities of 10^{18} and $10^{19} \text{ n}_e/\text{cc}$, particularly for the 50 μm CPC case as this is approx. 100 μm longer, the number of electrons that reach the highest energies appears to grow. The highest energy

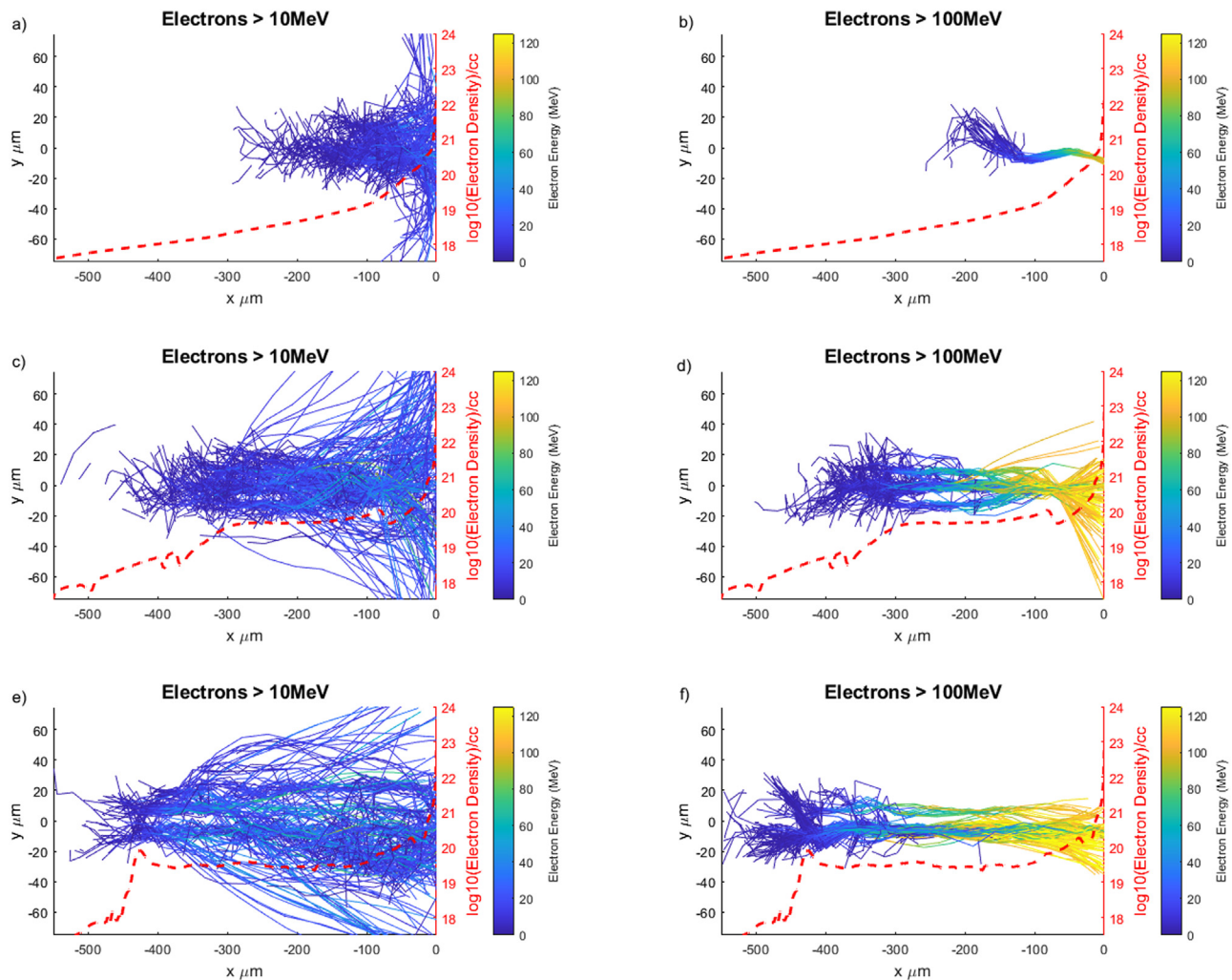


FIG. 12. Each line represents a tracked electron with the color of the line representing the energy. The plots are split into two columns, separated by the energy thresholds $> 10 \text{ MeV}$ [(a), (c), and (e)] and $> 100 \text{ MeV}$ [(b), (d), and (f)], and three rows, separated by the simulations of the flat [(a) and (b)], 50 μm CPC [(c) and (d)], and 25 μm CPC [(e) and (f)]. The electrons that reach the highest electron energies mostly travel along the regions of filaments. The right column of Fig. 11 shows the areas within the simulation box that the electrons gain energy. The long narrow regions in the right column of Fig. 11 correspond to the locations of the tracked electrons with the highest energies.

electron comes from the region after the density reaches 10^{19} n_e/cc . This demonstrates that the electrons further away from the target are capable of gaining the most energy.

As the tracked electrons travel through the simulation, they will lose and gain energies at specific locations. The energy difference and mean location between two outputs for each electron over the course of the entire simulation is calculated. The results are plotted in Figs. 11(b), 11(d), and 11(f) for the planar, 25 μm CPC, and 50 μm CPC, respectively. The electrons in each simulation are gaining much of their energy at the locations of the filaments. The accelerating regions also begin at the point of the density shelf for both cases.

Finally, we plot in Fig. 12 the electron energies (color of line) for 300 randomly selected electron as a function of position within the simulation for two conditions: electrons with energies greater than 10 MeV [(a), (c), and (e)] and greater than 100 MeV [(b), (d), and (f)]. For the flat target simulation, there are less than 300 electrons above 100 MeV; therefore, all are plotted instead of a random subset. The acceleration of the electron begins at densities between 10^{18} and 10^{19} n_e/cc , but the bulk of the acceleration occurs after 10^{19} n_e/cc . The electrons that remain within the regions of the laser filaments are capable of the gaining the most energy. We observe this for all simulations. However, it is much more likely that electrons can leave the region of acceleration gaining a modest amount of energy, which for all the electrons shown in Fig. 12 is much greater than the ponderomotive scaling/limit.

It is clear that the electrons that gain the most energy from these simulations all follow a few criteria. These electrons must be exposed to the highest intensities, which reside within self-focused filaments. Second, they must start accelerating as far away from the target as possible. This second criteria seems to suggest that the highest energy electron should, therefore, come from the densities prior to 10^{18} n_e/cc . Arefiev *et al.*¹⁶ showed that there is a threshold for the DLA to occur within the plasma that is described as $G \equiv a_0 \omega_p / \omega$, where a_0 is the normalized laser potential and ω and ω_p are the laser and plasma frequencies respectively. Here, G is referred to as the “gain” parameter. In a simple model where an electron is present in different plasma densities and exposed to different values of a_0 , the threshold for acceleration can be shown to be approximately $G = 1$. For a more realistic scenario, where the electron can be injected at any laser phase, the threshold is much lower, $G \approx 0.5$. For a laser intensity of 2×10^{19} W/cm^2 , $G = 0.5$ at an electron density of 2×10^{19} n_e/cc . This density agrees with the threshold at which we observe the starting locations of the highest electron energies. The simulations will also include many other effects that enhance the acceleration of the electrons such as the self-focusing of the laser to higher intensities with would lower the density limit in the gain equation.

VII. CONCLUSION

We have shown experimentally that large scale length plasma, generated, for example, by the intrinsic prepulse on Livermore’s Titan laser system in cone targets, is beneficial to the generation of electrons with energies much higher than the ponderomotive potential in the interaction of a picosecond scale relativistic laser pulse. Compared to the planar target, where the on-axis electron temperature was 5.7 MeV, the two CPCs, 25 and 50 μm tips, yield temperatures of 14.05 and 13.3 MeV, respectively. The number of on-axis electrons recorded has also increased by up to a factor of 3 from the planar to the 25 μm CPC.

CPCs have been shown previously at the Texas Petawatt to provide enhancement via intensification of the laser pulse.¹² However, at the Texas Petawatt, the pulse duration was short (150 fs) and the contrast, the difference between the laser peak power and laser pedestal was large. This led to little preplasma growth. Here, it was hypothesized that the average 17 mJ prepulse, 1.5 ns prior to the main pulse, generates a long enough plasma to nullify any focusing effects. Hydrodynamic and PIC simulations were conducted using the prepulse and target geometry to test this hypothesis. Using 3D HYDRA simulations with the experimentally measured prepulse into the CPC geometry, we observed the growth of a plasma that is denser than that of a planar target. This was due to combination of prepulse intensification and geometric confinement of the expanding plasma. The structure of the plasma within the CPCs was vastly different from a typical preplasma as it had a plateau at around $0.02n_c$. The simulated plasma densities were used as inputs for 2D PIC simulations. The simulated electron spectra for each target showed similar trends to the experimental data. The intensity at the tip of the CPCs showed no signs of geometric intensification, instead, the laser self-focuses and filaments into long channels. The combination of a long plasma and long filaments led to ideal conditions for DLA, leading to high energy electrons.

ACKNOWLEDGMENTS

The authors would like to thank the facility staff at the Jupiter Laser Facility for their help conducting the experiment. This work was supported by the DOE Office of Science, Fusion Energy Sciences under Contract Nos. DE-SC0019167 and SCW1575-1.

This work was performed under the auspices of the U.S. Department of Energy by Lawrence Livermore National Laboratory under Contract No. DE-AC52-07NA27344 and funded by the LLNL LDRD program under tracking code 19-SI-002 and NNSA Contract No. DE-NA0001808 for the target support from General Atomic (Release No. IM:LLNL-JRNL-839661-DRAFT).

AUTHOR DECLARATIONS

Conflict of Interest

The authors have no conflicts to disclose.

Author Contributions

Dean Richard Rusby: Conceptualization (lead); Data curation (lead); Formal analysis (lead); Investigation (lead); Methodology (lead); Visualization (lead); Writing – original draft (lead); Writing – review & editing (lead). **Nuno Lemos:** Investigation (equal); Methodology (equal). **Mario J.-E. Manuel:** Conceptualization (equal); Methodology (equal). **Tammy Ma:** Investigation (equal); Methodology (equal); Supervision (equal). **Andrew MacPhee:** Conceptualization (equal); Investigation (equal); Methodology (equal). **Isabella Mary Pagano:** Data curation (equal); Investigation (equal). **Arthur Pak:** Investigation (equal); Methodology (equal); Writing – review & editing (equal). **Graeme Gordon Scott:** Data curation (equal); Investigation (equal); Methodology (equal). **Craig W. Siders:** Conceptualization (equal); Funding acquisition (equal); Project administration (supporting). **Raspberry Antonia Simpson:** Investigation (equal); Methodology (equal). **Mitchell Sinclair:** Investigation (equal); Methodology (supporting); Writing – review & editing (supporting). **Scott Wilks:** Formal analysis (equal);

Visualization (equal); Writing – review & editing (equal). **Ginevra E. Cochran:** Formal analysis (equal); Investigation (equal); Visualization (equal); Writing – review & editing (equal). **Gerald Jackson Williams:** Data curation (equal); Formal analysis (equal); Investigation (equal); Writing – review & editing (equal). **Andy J. MacKinnon:** Funding acquisition (lead); Investigation (equal); Methodology (equal); Project administration (lead); Resources (lead); Supervision (lead); Writing – review & editing (equal). **Adeola C Aghedo:** Investigation (equal); Methodology (equal). **Felicie Albert:** Investigation (equal); Methodology (equal); Supervision (equal). **C D Armstrong:** Investigation (equal); Methodology (equal); Writing – review & editing (equal). **Alex Haid:** Methodology (equal). **Andreas J. Kemp:** Formal analysis (equal); Visualization (equal); Writing – review & editing (equal). **Shaun Kerr:** Investigation (equal); Methodology (equal); Writing – review & editing (equal). **Paul King:** Data curation (equal); Investigation (equal); Methodology (equal).

DATA AVAILABILITY

The data that support the findings of this study are available from the corresponding author upon reasonable request.

REFERENCES

- ¹O. Culfá, G. J. Tallents, A. K. Rossall, E. Wagenaars, C. P. Ridgers, C. D. Murphy, R. J. Dance, R. J. Gray, P. McKenna, C. D. Brown, S. F. James, D. J. Hoarty, N. Booth, A. P. Robinson, K. L. Lancaster, S. A. Pikuz, A. Y. Faenov, T. Kampfer, K. S. Schulze, I. Uschmann, and N. C. Woolsey, *Phys. Rev. E* **93**, 043201 (2016).
- ²P. McKenna, D. C. Carroll, O. Lundh, F. Nrnberg, K. Markey, S. Bandyopadhyay, D. Batani, R. G. Evans, R. Jafer, S. Kar, D. Neely, D. Pepler, M. N. Quinn, R. Redaelli, M. Roth, C. G. Wahlström, X. H. Yuan, and M. Zepf, *Laser Part. Beams* **26**, 591 (2008).
- ³J. Peebles, M. S. Wei, A. V. Arefiev, C. McGuffey, R. B. Stephens, W. Theobald, D. Haberberger, L. C. Jarrott, A. Link, H. Chen, H. S. McLean, A. Sorokovikova, S. Krashennnikov, and F. N. Beg, *New J. Phys.* **19**, 023008 (2017).
- ⁴A. Sorokovikova, A. V. Arefiev, C. McGuffey, B. Qiao, A. P. Robinson, M. S. Wei, H. S. McLean, and F. N. Beg, *Phys. Rev. Lett.* **116**, 155001 (2016).
- ⁵C. Courtois, A. Compant La Fontaine, O. Landoas, G. Lidove, V. ot, P. Morel, R. Nuter, E. Lefebvre, A. Boscheron, J. Grenier, M. M. Alonard, M. Gerbaux, F. Gobet, F. Hannachi, G. Malka, J. N. Scheurer, and M. Tarisien, *Phys. Plasmas* **16**, 013105 (2009).
- ⁶S. C. Wilks and W. L. Kruer, *IEEE J. Quantum Electron.* **33**(11), 1954–1968 (1997).
- ⁷M. G. Haines, M. S. Wei, F. N. Beg, and R. B. Stephens, *Phys. Rev. Lett.* **102**, 045008 (2009).
- ⁸F. N. Beg, A. R. Bell, A. E. Dangor, C. N. Danson, A. P. Fews, M. E. Glinsky, B. A. Hammel, P. Lee, P. A. Norreys, and M. Tatarakis, *Phys. Plasmas* **4**, 447 (1997).
- ⁹T. Tanimoto, H. Habara, R. Kodama, M. Nakatsutsumi, K. A. Tanaka, K. L. Lancaster, J. S. Green, R. H. Scott, M. Sherlock, P. A. Norreys, R. G. Evans, M. G. Haines, S. Kar, M. Zepf, J. King, T. Ma, M. S. Wei, T. Yabuuchi, F. N. Beg, M. H. Key, P. Nilson, R. B. Stephens, H. Azechi, K. Nagai, T. Norimatsu, K. Takeda, J. Valente, and J. R. Davies, *Phys. Plasmas* **16**, 062703 (2009).
- ¹⁰T. Kluge, S. A. Gaillard, K. A. Flippo, T. Burriss-Mog, W. Enghardt, B. Gall, M. Geissel, A. Helm, S. D. Kraft, T. Lockard, J. Metzkes, D. T. Offermann, M. Schollmeier, U. Schramm, K. Zeil, M. Bussmann, and T. E. Cowan, *New J. Phys.* **14**, 023038 (2012).
- ¹¹H. Chen, S. C. Wilks, W. L. Kruer, P. K. Patel, and R. Shepherd, *Phys. Plasmas* **16**, 020705 (2009).
- ¹²D. R. Rusby, P. M. King, A. Pak, N. Lemos, S. Kerr, G. Cochran, I. Pagano, A. Hannasch, H. Quevedo, M. Spinks, M. Donovan, A. Link, A. Kemp, S. C. Wilks, G. J. Williams, M. J.-E. Manuel, Z. Gavin, A. Haid, F. Albert, M. Aufderheide, H. Chen, C. W. Siders, A. MacPhee, and A. MacKinnon, *Phys. Rev. E* **103**, 053207 (2021).
- ¹³G. J. Williams, A. Link, M. Sherlock, D. A. Alessi, M. Bowers, B. P. Golick, M. Hamamoto, M. R. Hermann, D. Kalantar, K. N. Lafortune, A. J. MacKinnon, A. MacPhee, M. J. Manuel, D. Martinez, M. Mauldin, L. Pelz, M. Prantil, M. Quinn, B. Remington, R. Sigurdsson, P. Wegner, K. Youngblood, and H. Chen, *Phys. Rev. E* **103**, 031201 (2021), [arXiv:2012.11563](https://arxiv.org/abs/2012.11563).
- ¹⁴D. Raffestin, L. Lecherbourg, I. Lantuéjoul, B. Vauzour, P. E. Masson-Laborde, X. Davoine, N. Blanchot, J. L. Dubois, X. Vaisseau, E. D’Humières, L. Gremillet, A. Duval, C. Reverdin, B. Rosse, G. Boutoux, J. E. Ducret, C. Rousseaux, V. Tikhonchuk, and D. Batani, *Matter Radiat. Extremes* **6**, 056901 (2021).
- ¹⁵R. A. Simpson, G. G. Scott, D. Mariscal, D. Rusby, P. M. King, E. Grace, A. Aghedo, I. Pagano, M. Sinclair, C. Armstrong, M. J. Manuel, A. Haid, K. J. Flippo, L. Winslow, M. Gatu-Johnson, J. A. Frenje, D. Neely, S. Kerr, G. J. Williams, S. Andrews, R. Cauble, K. Charron, R. Costa, B. Fischer, S. Maricle, B. Stuart, F. Albert, N. Lemos, A. MacKinnon, A. MacPhee, A. Pak, and T. Ma, *Phys. Plasmas* **28**, 013108 (2021).
- ¹⁶A. V. Arefiev, V. N. Khudik, A. P. Robinson, G. Shvets, L. Willingale, and M. Schollmeier, *Phys. Plasmas* **23**, 056704 (2016), [arXiv:1602.08758](https://arxiv.org/abs/1602.08758).
- ¹⁷A. P. Robinson, A. V. Arefiev, and D. Neely, *Phys. Rev. Lett.* **111**, 065002 (2013), [arXiv:1303.0233](https://arxiv.org/abs/1303.0233).
- ¹⁸A. J. Kemp and S. C. Wilks, *Phys. Plasmas* **27**, 103106 (2020).
- ¹⁹A. Pukhov, Z. M. Sheng, and J. Meyer-ter Vehn, *Phys. Plasmas* **6**, 2847 (1999).
- ²⁰S. Kojima, M. Hata, N. Iwata, Y. Arikawa, A. Morace, S. Sakata, S. Lee, K. Matsuo, K. F. F. Law, H. Morita, Y. Ochiai, A. Yogo, H. Nagatomo, T. Ozaki, T. Johzaki, A. Sunahara, H. Sakagami, Z. Zhang, S. Tosaki, Y. Abe, J. Kawanaka, S. Tokita, M. Nakai, H. Nishimura, H. Shiraga, H. Azechi, Y. Sentoku, and S. Fujioka, *Commun. Phys.* **2**, 99 (2019).
- ²¹A. G. Krygier, D. W. Schumacher, and R. R. Freeman, *Phys. Plasmas* **21**, 023112 (2014).
- ²²C. Courtois, R. Edwards, A. Compant La Fontaine, C. Aedy, M. Barbotin, S. Bazzoli, L. Biddle, D. Brebion, J. L. Bourgade, D. Drew, M. Fox, M. Gardner, J. Gazave, J. M. Lagrange, O. Landoas, L. Le Dain, E. Lefebvre, D. Mastro Simone, N. Pichoff, G. Pien, M. Ramsay, A. Simons, N. Sircombe, C. Stoeckl, and K. Thorp, *Phys. Plasmas* **18**, 023101 (2011).
- ²³A. C. L. Fontaine, C. Courtois, F. Gobet, F. Hannachi, J. R. Marquès, M. Tarisien, M. Versteegen, and T. Bonnet, *Phys. Plasmas* **26**, 113109 (2019).
- ²⁴H. Sawada, C. M. Salinas, F. N. Beg, H. Chen, A. J. Link, H. S. McLean, P. K. Patel, Y. Ping, and G. J. Williams, *Plasma Phys. Controlled Fusion* **62**, 065001 (2020).
- ²⁵D. R. Rusby, C. M. Brenner, C. Armstrong, L. A. Wilson, R. Clarke, A. Alejo, H. Ahmed, N. M. H. Butler, D. Haddock, A. Higginson, A. McClymont, S. R. Mirfayzi, C. Murphy, M. Notley, P. Oliver, R. Allott, C. Hernandez-Gomez, S. Kar, P. McKenna, and D. Neely, *Proc. SPIE* **9992**, 99920E (2016).
- ²⁶C. D. Armstrong, C. M. Brenner, C. Jones, D. R. Rusby, Z. E. Davidson, Y. Zhang, J. Wragg, S. Richards, C. Spindloe, P. Oliveira, M. Notley, R. Clarke, S. R. Mirfayzi, S. Kar, Y. Li, T. Scott, P. McKenna, and D. Neely, *High Power Laser Sci. Eng.* **7**, e24 (2019).
- ²⁷H. Daido, M. Nishiuchi, and A. S. Pirozhkov, “Review of laser-driven ion sources and their applications,” *Rep. Prog. Phys.* **75**(5), 056401 (2012).
- ²⁸J. Fuchs, P. Antici, E. D’Humières, E. Lefebvre, M. Borghesi, E. Brambrink, C. A. Cecchetti, M. Kaluza, V. Malka, M. Manclossi, S. Meyroneinc, P. Mora, J. Schreiber, T. Toncian, H. Pépin, and P. Audebert, *Nat. Phys.* **2**, 48 (2006).
- ²⁹P. Mora, *Phys. Rev. Lett.* **90**, 185002 (2003).
- ³⁰A. E. Hussein, A. V. Arefiev, T. Batson, H. Chen, R. S. Craxton, A. S. Davies, D. H. Froula, Z. Gong, D. Haberberger, Y. Ma, P. M. Nilson, W. Theobald, T. Wang, K. Weichman, G. J. Williams, and L. Willingale, *New J. Phys.* **23**, 023031 (2021), [arXiv:2101.07211](https://arxiv.org/abs/2101.07211).
- ³¹Y. Sentoku, K. Mima, H. Ruhl, Y. Toyama, R. Kodama, and T. E. Cowan, *Phys. Plasmas* **11**, 3083 (2004).
- ³²A. G. MacPhee, L. Divol, A. J. Kemp, K. U. Akli, F. N. Beg, C. D. Chen, H. Chen, D. S. Hey, R. J. Fedosejevs, R. R. Freeman, M. Hennesian, M. H. Key, S. Le Pape, A. Link, T. Ma, A. J. MacKinnon, V. M. Ovchinnikov, P. K. Patel, T. W. Phillips, R. B. Stephens, M. Tabak, R. Town, Y. Y. Tsui, L. D. Van Woerkom, M. S. Wei, and S. C. Wilks, *Phys. Rev. Lett.* **104**, 055002 (2010).
- ³³T. Ma, H. Sawada, P. K. Patel, C. D. Chen, L. Divol, D. P. Higginson, A. J. Kemp, M. H. Key, D. J. Larson, S. Le Pape, A. Link, A. G. MacPhee, H. S. McLean, Y. Ping, R. B. Stephens, S. C. Wilks, and F. N. Beg, *Phys. Rev. Lett.* **108**, 115004 (2012).

- ³⁴H. Hinterberger and R. Winston, "Efficient light coupler for threshold Čerenkov counters," *Rev. Sci. Instrum.* **37**, 1094 (1966).
- ³⁵A. G. MacPhee, D. Alessi, H. Chen, G. Cochran, M. R. Hermann, D. H. Kalantar, A. J. Kemp, S. M. Kerr, A. J. Link, T. Ma, A. J. Mackinnon, D. A. Mariscal, D. Schlossberg, R. Tommasini, S. Vonhof, C. C. Widmayer, S. C. Wilks, G. J. Williams, W. H. Williams, and K. Youngblood, *Optica* **7**, 129 (2020).
- ³⁶G. E. Cochran, A. J. Kemp, S. C. Wilks, S. M. Kerr, G. J. Williams, D. A. Alessi, J. G. D. Nicola, M. R. Hermann, D. H. Kalantar, T. E. Lanier, M. M. Marinak, D. Martinez, M. A. Prantil, C. Widmayer, W. H. Williams, and A. J. Mackinnon, *Phys. Plasma* **28**, 113106 (2021).
- ³⁷S. Le Pape, Y. Y. Tsui, A. MacPhee, D. Hey, P. Patel, A. Mackinnon, M. Key, M. Wei, T. Ma, F. N. Beg, R. Stephens, K. Akli, T. Link, L. Van-Woerkom, and R. R. Freeman, *Opt. Lett.* **34**, 2997 (2009).
- ³⁸T. Bonnet, M. Comet, D. Denis-Petit, F. Gobet, F. Hannachi, M. Tarisien, M. Versteegen, and M. M. Aléonard, *Rev. Sci. Instrum.* **84**, 103510 (2013).
- ³⁹A. Link, R. R. Freeman, D. W. Schumacher, and L. D. Van Woerkom, *Phys. Plasmas* **18**, 053107 (2011).
- ⁴⁰D. R. Rusby, C. D. Armstrong, G. G. Scott, M. King, P. McKenna, and D. Neely, *High Power Laser Sci. Eng.* **7**, e45 (2019).
- ⁴¹R. J. Gray, X. H. Yuan, D. C. Carroll, C. M. Brenner, M. Coury, M. N. Quinn, O. Tresca, B. Zielbauer, B. Aurand, V. Bagnoud, J. Fils, T. Kühn, X. X. Lin, C. Li, Y. T. Li, M. Roth, D. Neely, and P. McKenna, *Appl. Phys. Lett.* **99**, 171502 (2011).
- ⁴²D. R. Rusby, L. A. Wilson, R. J. Gray, R. Dance, N. M. H. Butler, D. A. MacLellan, G. G. Scott, V. Bagnoud, B. Zielbauer, P. McKenna, and D. Neely, "Measurement of the angle, temperature and flux of fast electrons emitted from intense laser–solid interactions," *J. Plasma Phys.* **81**, 475810505 (2015).
- ⁴³M. A. Stoyer, T. C. Sangster, E. A. Henry, M. D. Cable, T. E. Cowan, S. P. Hatchett, M. H. Key, M. J. Moran, D. M. Pennington, M. D. Perry, T. W. Phillips, M. S. Singh, R. A. Snively, M. Tabak, and S. C. Wilks, *Rev. Sci. Instrum.* **72**, 767 (2001).
- ⁴⁴M. I. K. Santala, M. Zepf, I. Watts, F. N. Beg, E. Clark, M. Tatarakis, K. Krushelnick, A. E. Dangor, T. Mccanny, I. Spencer, R. P. Singhal, K. W. D. Ledingham, S. C. Wilks, A. C. Machacek, J. S. Wark, R. Allott, R. J. Clarke, and P. A. Norreys, "Effect of the plasma density scale length on the direction of fast electrons in relativistic laser–solid interactions," *Phys. Rev. Lett.* **84**(7), 1459–1462 (2000).
- ⁴⁵G. J. Williams, A. Link, M. Sherlock, D. A. Alessi, M. Bowers, A. Conder, P. Di Nicola, G. Fiksel, F. Fiuza, M. Hamamoto, M. R. Hermann, S. Herriot, D. Homoelle, W. Hsing, E. D'Humières, D. Kalantar, A. Kemp, S. Kerr, J. Kim, K. N. Lafortune, J. Lawson, R. Lowe-Webb, T. Ma, D. A. Mariscal, D. Martinez, M. J. Manuel, M. Nakai, L. Pelz, M. Prantil, B. Remington, R. Sigurdsson, C. Widmayer, W. Williams, L. Willingale, R. Zacharias, K. Youngblood, and H. Chen, *Phys. Rev. E* **101**, 031201(R) (2020).
- ⁴⁶N. P. Dover, M. Nishiuchi, H. Sakaki, K. Kondo, M. A. Alkhimova, A. Y. Faenov, M. Hata, N. Iwata, H. Kiriya, J. K. Koga, T. Miyahara, T. A. Pikuz, A. S. Pirozhkov, A. Sagisaka, Y. Sentoku, Y. Watanabe, M. Kando, and K. Kondo, *Phys. Rev. Lett.* **124**, 84802 (2020).